UC Berkeley
UC Berkeley Previously Published Works

Title

Perovskite-driven solar C2 hydrocarbon synthesis from CO2

Permalink

https://escholarship.org/uc/item/3s03b33k

Journal

Nature Catalysis, 8(2)

ISSN

2520-1158

Authors

Andrei, Virgil

Roh, Inwhan

Lin, Jia-An

et al.

Publication Date

2025-02-01

DOI

10.1038/s41929-025-01292-y

Copyright Information

Peer reviewed

Perovskite-driven solar C_2 hydrocarbon synthesis from CO_2

Virgil Andrei [1,2,3,4,8] ✉, Inwhan Roh [1,5,8], Jia-An Lin [1,5], Joshua Lee[1], Yu Shan [6], Chung-Kuan Lin[1], Steve Shelton[2], Erwin Reisner [3] & Peidong Yang [1,5,6,7] ✉

Photoelectrochemistry (PEC) presents a direct pathway to solar fuel synthesis by integrating light absorption and catalysis into compact electrodes. Yet, PEC hydrocarbon production remains elusive due to high catalytic overpotentials and insufficient semiconductor photovoltage. Here we demonstrate ethane and ethylene synthesis by interfacing lead halide perovskite photoabsorbers with suitable copper nanoflower electrocatalysts. The resulting perovskite photocathodes attain a 9.8% Faradaic yield towards C_2 hydrocarbon production at 0 V against the reversible hydrogen electrode. The catalyst and perovskite geometric surface areas strongly influence C_2 photocathode selectivity, which indicates a role of local current density in product distribution. The thermodynamic limitations of water oxidation are overcome by coupling the photocathodes to Si nanowire photoanodes for glycerol oxidation. These unassisted perovskite–silicon PEC devices attain partial C_2 hydrocarbon photocurrent densities of 155 µA cm^{-2}, 200-fold higher than conventional perovskite–BiVO$_4$ artificial leaves for water and CO_2 splitting. These insights establish perovskite semiconductors as a versatile platform towards PEC multicarbon synthesis.

C_2 hydrocarbons such as ethane and ethylene are major industrial feedstocks for plastics synthesis, with ethylene production exceeding that of any other organic chemical[1]. However, they are exclusively sourced or produced from fossil resources including natural gas or naphtha[1]. Photoelectrochemistry (PEC) presents a sustainable alternative towards direct C_2 hydrocarbon production from small building blocks such as CO_2 or H_2O. These light-driven systems can reduce costs by integrating light harvesting and catalysis into a single panel that operates under benign conditions[2,3], as well as mitigating the intermediate steps and CO_2 emissions from industrial processes (Supplementary Note 1)[1,4].

Despite substantial progress on the electrochemical CO_2 reduction reaction (CO$_2$RR) in gas flow cells[5–7], examples of PEC C_2 hydrocarbon synthesis remain sparse[8,9]. This can be traced back to a limited choice of

catalysts for C_2 product formation (only copper-based compounds)[10,11], high overpotentials of 0.5–0.8 V for electrochemical hydrocarbon synthesis[12,13], and photovoltages below 0.7 V of established semiconductors including Si (ref. 14), III–V compounds[15] or oxides[16–18]. As a result, unassisted hydrocarbon synthesis is demonstrated only as trace amounts in PEC tandem devices reaching partial photocurrent densities below 20 µA cm^{-2} for C_{2+} alcohols[19]. One emerging approach to reduce the required photovoltage is by replacing the thermodynamically demanding O_2 evolution reaction (OER) by more facile organic oxidations. For instance, the glycerol oxidation reaction (GOR) can alleviate the photovoltage requirement by 1 V, while converting a biomass-derived waste product into value-added chemicals for the pharmaceutical, food and cosmetic industries[20,21].

[1]Department of Chemistry, University of California, Berkeley, Berkeley, CA, USA. [2]Molecular Foundry, Lawrence Berkeley National Laboratory, Berkeley, CA, USA. [3]Yusuf Hamied Department of Chemistry, University of Cambridge, Cambridge, UK. [4]Optoelectronics Group, Cavendish Laboratory, University of Cambridge, Cambridge, UK. [5]Liquid Sunlight Alliance, Lawrence Berkeley National Laboratory, Berkeley, CA, USA. [6]Department of Materials Science and Engineering, University of California, Berkeley, Berkeley, CA, USA. [7]Kavli Energy Nanosciences Institute, Berkeley, CA, USA. [8]These authors contributed equally: Virgil Andrei, Inwhan Roh. ✉e-mail: va291@cam.ac.uk; p_yang@berkeley.edu

Here we demonstrate C_2 hydrocarbon formation by interfacing low-overpotential Cu electrocatalysts with perovskite light absorbers with 1 V photovoltage. These buried-junction photocathodes reveal an interplay between electron flux, applied potential and C_2 selectivity, which manifests when assembling unassisted PEC devices. Accordingly, tandem devices with robust $BiVO_4$ and TiO_2 photoanodes couple aqueous ethane and ethylene production with O_2 evolution. The C_2 partial current densities are improved 200-fold by wiring the perovskite photocathodes to Si photoanodes for GOR, providing a proof-of-concept demonstration for simultaneous PEC hydrocarbon and organic synthesis.

Results

Cu nanoflower electrochemistry

A copper nanoflower (Cu_{NF}) electrocatalyst was optimized for CO_2 reduction based on its promising activity towards ethylene synthesis[22,23] and its compatibility with our overall system design (see Supplementary Fig. 1 for the results of our initial catalyst screening). The catalyst was obtained by surface oxidation of Cu foil in an alkaline ammonium persulfate solution. This resulted in the growth of CuO nanoflowers, which were subsequently electroreduced to metallic Cu_{NF} (Methods). The catalyst consisted of 2–4-µm-wide clusters, which preserved the 50-nm-thin nanoplatelet structure of CuO (Fig. 1 and Supplementary Figs. 2 and 3). Such hierarchical, porous structures are known to promote CO_2 reduction by increasing the local pH and, hence, reducing the availability of protons for the competing H_2 evolution[24,25].

Although previous studies considered only CO electroreduction under strongly basic pH (refs. 22,23), CO_2 conversion photoelectrodes often operate under benign conditions. Hence, the catalytic activity of Cu_{NF} was first screened in an aqueous 0.1 M $KHCO_3$ solution, under constant CO_2 flow (Fig. 2, Supplementary Fig. 4 and Supplementary Table 1). Traces of ethane and ethylene could be observed already at −0.5 V versus reversible hydrogen electrode (RHE) (Faradaic yield (FY) <1%), which makes the catalyst compatible with state-of-the-art tandem PEC devices for unassisted CO_2 conversion[26,27]. The C_2 FY increased steadily at more negative applied potentials, plateauing around 10% below −0.9 V versus RHE. While most electrocatalytic studies target specifically C_2H_4 and C_2H_5OH, the formation of C_2H_6 has also been reported for oxide-derived Cu catalysts[28], whereas the FY of C_2H_6 increases with the thickness of the catalyst layer[10]. Accordingly, it has been hypothesized that a thick, dense catalyst nanostructure like that of Cu_{NF} favours C_2H_6 production, which is probably caused by the readsorption and further reduction of C_2H_4 (Fig. 1b)[10,29,30]. Alternatively, *CH_3 dimerization or ethoxy intermediates may also contribute to C_2H_6 formation[31].

CO constituted the major gaseous CO_2 reduction product at −0.5 V versus RHE (29% FY), whereas its proportion decreased substantially (FY <5%) at negative potentials favouring C_2 formation. This behaviour is also consistent with literature, as the more facile CO and formate production occurs at lower overpotentials of 0.1–0.3 V (refs. 10,13). The H_2 FY amounted to 30–60% depending on the applied potential. Similar trends in the FYs of gas products were observed under stepwise change of the applied potential (Supplementary Fig. 5 and Supplementary Table 2). The remaining FY can be traced back to liquid products such as formate (up to 36% FY) and small amounts of alcohols (3–7% FY) as determined from nuclear magnetic resonance (NMR)[32], whereas gas leakage from the PEC cell accounts for small deviations from the ideal 100% (Supplementary Figs. 4 and 6, and Supplementary Tables 1 and 3).

While Cu nanoparticle catalysts undergo structural transformations under negative applied potential[12,33,34], our data indicated that the nanoflower catalyst is robust to surface reoxidation under open-circuit conditions or positive potentials (postcatalysis scanning electron microscopy (SEM) characterization is shown in Supplementary Fig. 2g–i). This was further supported by a long-term stability test of a Cu_{NF} electrode, which revealed no substantial change in selectivity or morphology over three 12 h cycles (Supplementary Figs. 2j–l and 23).

This resilience to structural changes is desirable in real-world PEC systems under intermittent light irradiation[27,35]. Accordingly, CuO samples reduced either in advance, under subsequent cyclic voltammetry (CV) scans or under continuous controlled potential electrolysis (CPE) displayed a similar electrocatalytic behaviour within experimental error (Supplementary Fig. 5). This is consistent with X-ray diffraction (XRD) and X-ray photoelectron spectroscopy data, which indicated the presence of a surface oxide layer for both pristine CuO and Cu nanoflower electrodes ex situ (Supplementary Figs. 7 and 8).

Perovskite|Cu_{NF} photocathodes

The Cu nanoflower catalyst was next interfaced to perovskite PV devices via graphite epoxy paste[27] to form buried-junction photocathodes (abbreviated PVK|Cu_{NF}). The exposed edges and wiring were sealed by epoxy[26], which was also used to define the catalyst active area (Methods). PV devices with photoactive areas of ~25 mm² used a triple-cation mixed-halide perovskite light absorber that was sandwiched between hole and electron selective layers for effective charge separation (Fig. 1 and Supplementary Fig. 9). Those devices provided a high average open-circuit voltage (V_{OC}) of 1.08 ± 0.03 V, which is necessary to bias the Cu electrode for C_2 hydrocarbon formation (current–voltage (J–V) curves and histograms are shown in Supplementary Figs. 10 and 11). Accordingly, the photocathode performance was evaluated by CPE at 0 V versus RHE, which resembles the −0.9 V versus RHE potential applied during Cu electrocatalysis (Supplementary Fig. 12).

A strong dependence was observed in the C_2 selectivity of the integrated photocathodes with the exposed geometric area of the catalyst (Fig. 3, Supplementary Figs. 13 and 43, Supplementary Table 5 and Supplementary Note 2). Accordingly, the optimal selectivity towards ethane and ethylene production was obtained for a catalyst active area of ~4 mm², where the C_2 hydrocarbon FY amounted to 9.8% as expected from electrocatalysis. This smaller Cu_{NF} area may present practical benefits, as described in Supplementary Fig. 14. However, the C_2 hydrocarbon FY decreased steeply to 0.8% for a catalyst geometric area of 40 mm². This finding indicates that the current density influences selectivity, as noted in recent studies[13,26,27,36]. To rationalize this finding, CPE and CV scans were conducted for PVK|Cu_{NF} photocathodes and corresponding Cu_{NF} electrodes with varying catalyst geometric areas (Fig. 3, Supplementary Figs. 13 and 15–17 and Supplementary Tables 4 and 5). As expected, C_2 FYs remained similar across Cu_{NF} electrodes of different sizes. Meanwhile, CV scans indicated that an optimal selectivity is obtained when the absolute photocathode current (I) matches the one from electrochemistry (Fig. 3a). In other words, the photocurrent density through the catalyst (J_{cat}) needs to match the current density for Cu_{NF} electrodes of equivalent area (J_{Cu}) (Supplementary Figs. 15 and 17).

This current matching requirement defines two distinct regions within the CV plot (Fig. 3a). When the catalyst area is too small, the total photocurrent (I) is limited by catalysis. This means that the light absorber must force charges through a smaller catalyst area, resulting in relatively higher current densities ($J_{cat} > J_{Cu}$) (Supplementary Figs. 15c–e and 17b). However, when the catalyst surface area is too large, the current becomes limited by the charge generation through the light absorber. This perovskite photocurrent plateaus following the typical shape of a J–V curve[37,38], resulting in $J_{cat} < J_{Cu}$. This presents an unusual handle to fine-tune PEC product selectivity, which is often neglected when assembling such integrated or buried-junction photoelectrodes.

In terms of product distribution, the selectivity resembled the findings from electrochemistry, with formate amounting to 20–30% FY, and other C_{2+} liquid products (for example, ethanol) amounting to <10% FY over 2 h CPE at 0 V versus RHE (Supplementary Fig. 6). Photocathodes tested under different applied potentials also followed similar trends in the FY of C_2 hydrocarbon products as the dark Cu_{NF} electrodes (Figs. 2 and 4, Supplementary Fig. 18 and Supplementary Table 6). Lower C_2 FYs were attained during CPE in a more concentrated,
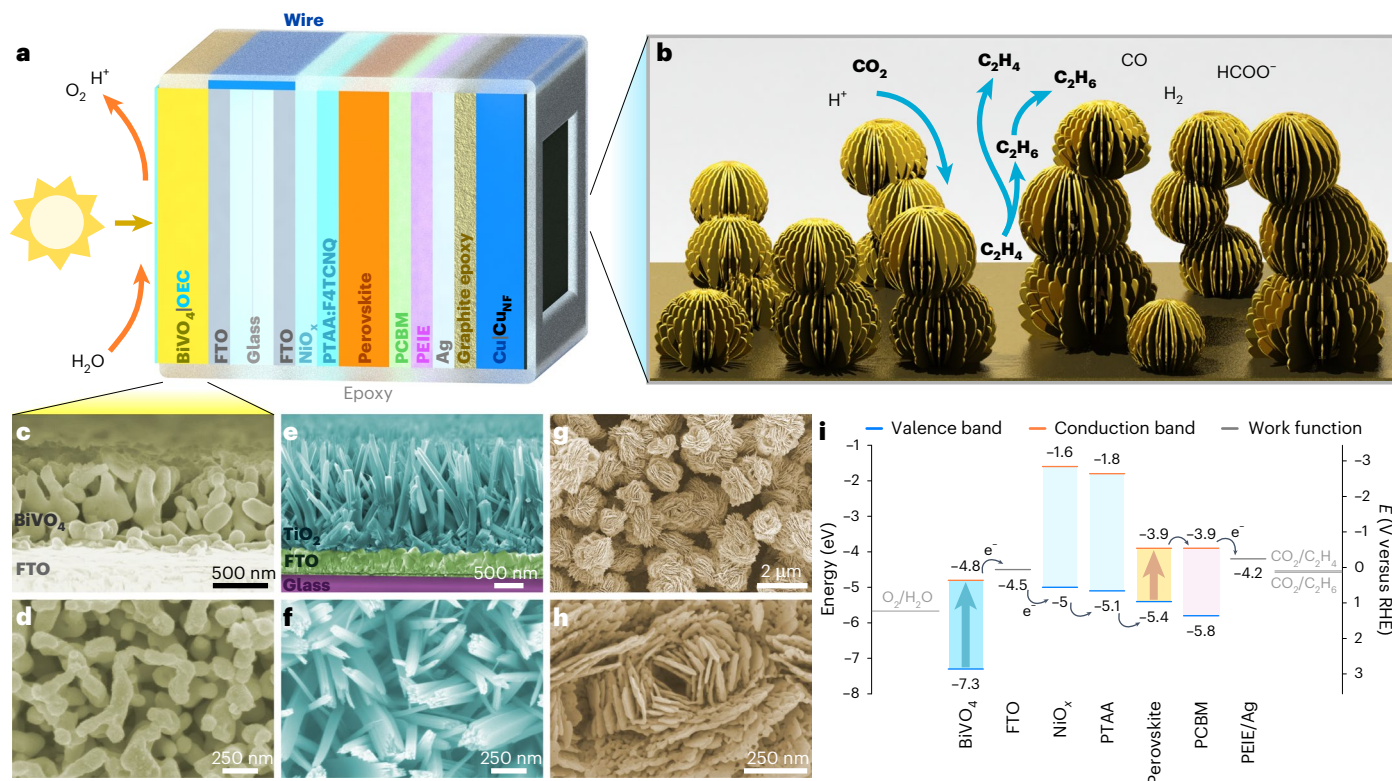
Fig. 1 | Design of a perovskite–BiVO₄ artificial leaf device towards unassisted C₂ hydrocarbon synthesis. a, Architecture of the tandem PEC device. **b**, A schematic illustration of the nanoporous electrode. **c–h**, False-colour SEM images of BiVO₄ (**c** and **d**), TiO₂ (**e** and **f**) and Cu$_{NF}$ (**g** and **h**). **c**,**e**, Cross-section images. **d**,**f–h**, Top views at different magnifications. The SEM images reveal a hierarchical catalyst nanostructure. **i**, Energy levels within a perovskite–BiVO₄ tandem device.
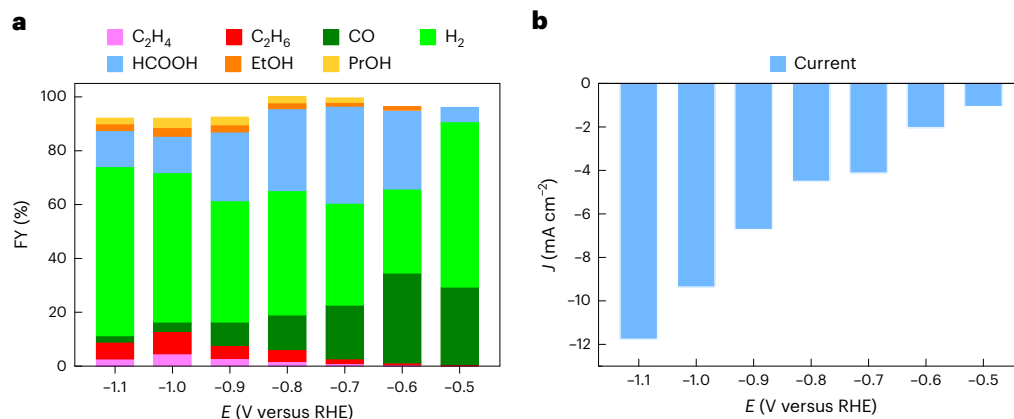

Fig. 2 | Selectivity of Cu nanoflower catalysts towards CO₂ reduction. a, FYs. **b**, Current densities. Two-hour CPE is conducted in a stirred 0.1 M KHCO₃ electrolyte (pH 6.8), under 5 sccm CO₂ flow, at room temperature.

0.5 M KHCO₃ electrolyte solution. Its buffering effect may prevent a higher local pH build-up, which is expected to favour C₂ formation (Supplementary Fig. 19 and Supplementary Table 5)[10,39].

^{13}C gas chromatography–mass spectrometry (GC–MS) experiments revealed that all gaseous products originate from CO₂ reduction (Fig. 3d and Supplementary Fig. 20). Small quantities of ^{12}C impurities were observed among liquid products (Supplementary Figs. 6 and 21), which probably originate from the epoxy resin used for encapsulation. While formate impurities amount to 5–10% of the total HCOO⁻ amounts, FYs are much more sensitive to small amounts of methanol and propanol (6 e⁻ and 18 e⁻ required for CO₂ reduction, respectively). Because all effective moisture encapsulation methods based on epoxy

resins resulted in liquid impurities (albeit in different compositions and ratios), we plot only the data for formate as the major liquid product.

Further controls indicated that photocathodes lose most activity within a few hours, with only traces of C₂ hydrocarbons noticeable beyond the first 12 h. While the perovskite device sustained a similar photocurrent, catalyst deactivation meant that most charges contribute towards H₂ evolution (Supplementary Fig. 22 and Supplementary Table 7). By contrast, a bare Cu$_{NF}$ catalyst sustained ethylene production over 36 h (Supplementary Fig. 23). This indicates that carbon impurities from the epoxy resin may deactivate the catalyst surface of the encapsulated photocathodes[40], which is consistent with earlier reports of Cu-based, buried-junction photocathodes[16].
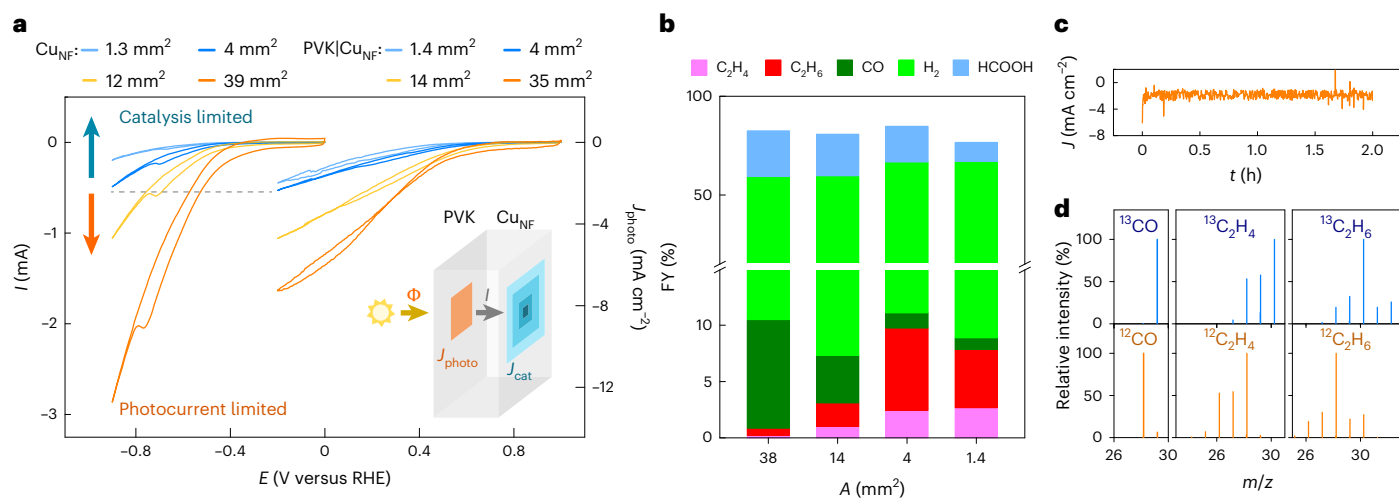
Fig. 3 | Catalyst-area dependent C$_2$ hydrocarbon selectivity for PVK|Cu$_{NF}$ photocathodes. a, CV traces of Cu$_{NF}$ electrodes of different sizes (left) and perovskite photocathodes with corresponding catalyst areas (right). The absolute photocurrent (*I*) is limited by either Cu$_{NF}$ electrocatalysis or perovskite light absorption. The inset illustrates the different photocurrent densities experienced by the light absorber (*J*$_{photo}$) and catalyst (*J*$_{cat}$), based on their respective areas. *Φ* represents the photon flux, which is ideally proportional to the perovskite photocurrent. **b**, FYs of the photocathodes, as a function of the catalyst geometric area. The optimal ethane and ethylene production is achieved when the absolute photocurrent matches that of Cu$_{NF}$ electrodes. **c**, CPE trace of the optimized perovskite photocathode with a 4 mm^2 Cu$_{NF}$ area. **d**, GC–MS isotopic labelling confirms that gaseous products originate from CO$_2$ reduction (residual N$_2$ and O$_2$ peaks are removed for clarity). Two-hour CPE is performed at 0 V versus RHE in a stirred 0.1 M KHCO$_3$ electrolyte (pH 6.8), under simulated 1 sun irradiation (AM1.5 G, 100 mW cm^{-2}), at room temperature.
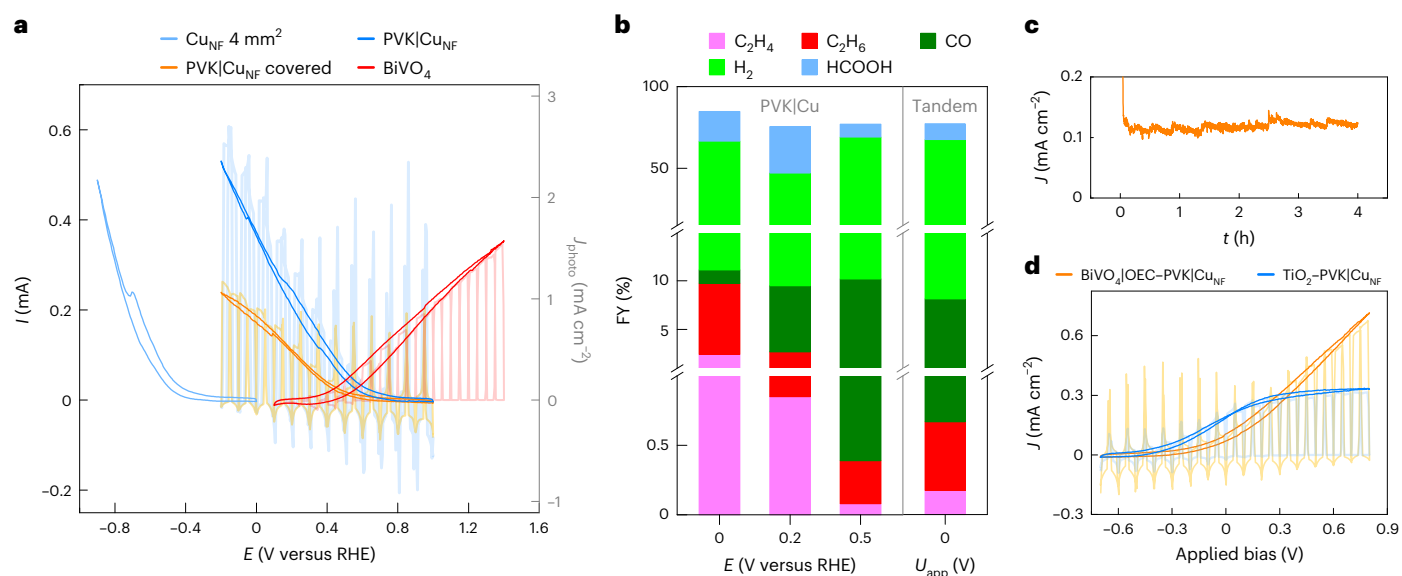

Fig. 4 | Perovskite|Cu$_{NF}$–BiVO$_4$ tandem devices coupling unassisted C$_2$ hydrocarbon production and O$_2$ evolution. a, CV traces of a Cu$_{NF}$ electrode, PVK|Cu$_{NF}$ photocathodes and a BiVO$_4$ photoanode. The perovskite photovoltage shifts the CV of the current-matched photocathode by 1 V over the corresponding dark electrode. A ~50% reduction in photocurrent is observed when placing the photocathode behind BiVO$_4$, in a back-to-back tandem PEC configuration. The sign of the cathodic traces is reversed to emphasize the current overlap. **b**, FYs of a BiVO$_4$|OEC–PVK|Cu$_{NF}$ tandem device at 0 V applied bias voltage (*U*$_{app}$) are compared with those of PVK|Cu$_{NF}$ photocathodes under different applied potentials. Axis breaks are used to visualize the FYs of C$_2$ products. **c**, The corresponding CPE of the perovskite–BiVO$_4$ tandem. **d**, CV traces of perovskite tandems with BiVO$_4$ and TiO$_2$. CPE is performed in a stirred 0.1 M KHCO$_3$ electrolyte (pH 6.8), under 1 sun irradiation (AM1.5 G, 100 mW cm^{-2}), at room temperature. In **a** and **d**, lighter shades indicate chopped light CV traces.

Artificial leaves for water and CO$_2$ splitting

Optimized perovskite photocathodes with a ~4 mm^2 Cu$_{NF}$ area were next interfaced to BiVO$_4$ and TiO$_2$ photoanodes for O$_2$ evolution, to assess the activity of tandem artificial leaves towards unassisted C$_2$ hydrocarbon production (Fig. 1a). BiVO$_4$ photoanodes were synthesized by electrodeposition of BiOI on fluorine-doped tin oxide (FTO) glass, followed by annealing in the presence of VO(acac)$_2$ (acac, acetylacetonate), whereas a spin-coated amorphous TiCoO$_x$ layer acted as the oxygen evolution catalyst (OEC)[27,41]. Alternatively, nanowire (NW) TiO$_2$ photoanodes were obtained by hydrothermal synthesis[42]. SEM and XRD data confirmed the successful fabrication of the desired nanostructured photoanodes (Supplementary Figs. 24 and 25).

CV traces of PVK|Cu$_{NF}$ and BiVO$_4$ photoelectrodes overlapped at a potential of ~0.5 V versus RHE, revealing that the system can operate under bias-free conditions. As perovskite devices provide 1 V photovoltage, this working potential corresponds to an applied potential
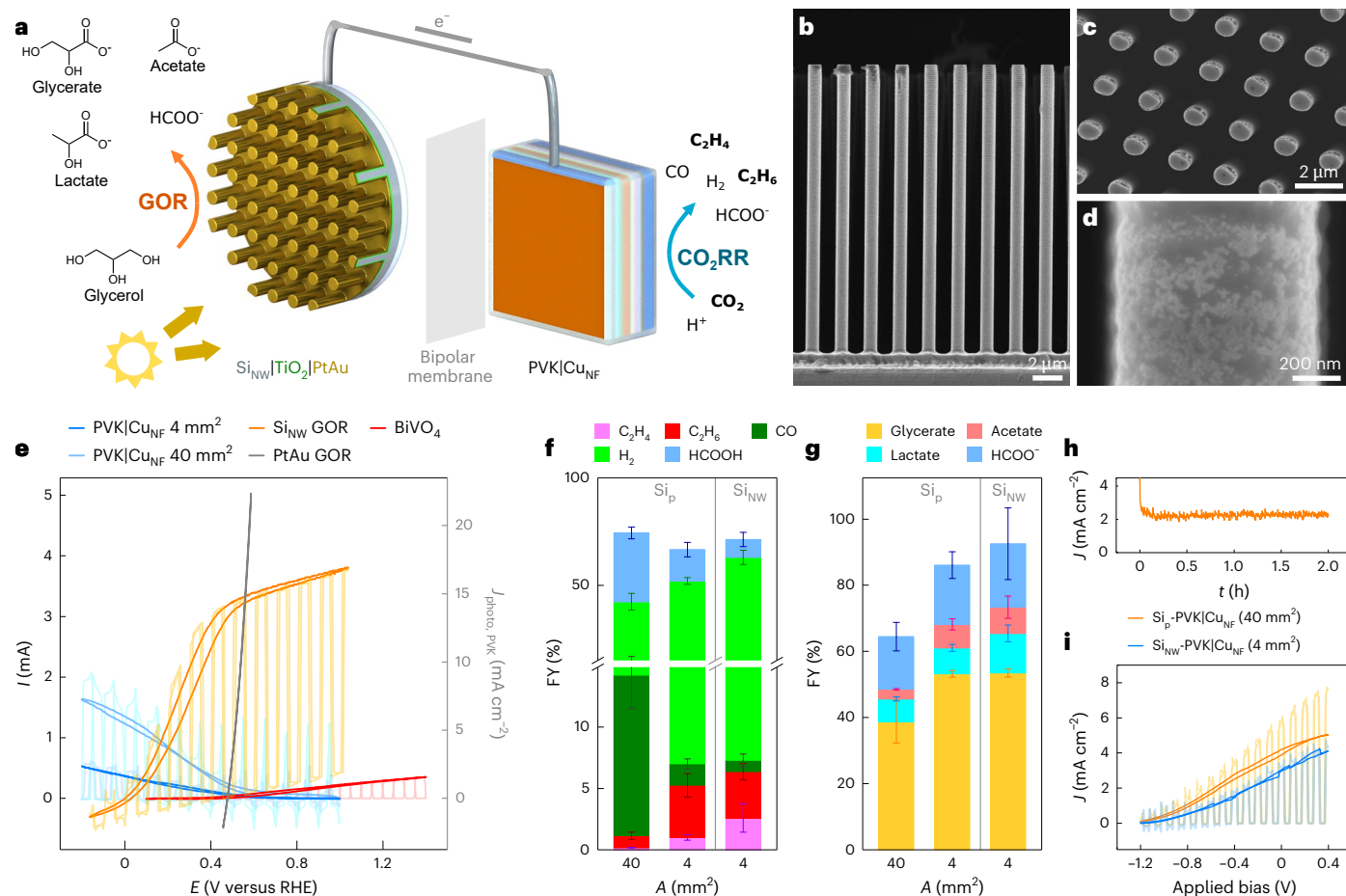
Fig. 5 | Perovskite|Cu$_{NF}$–Si PEC devices coupling unassisted C$_2$ hydrocarbon synthesis to GOR. a, A schematic illustration of the PEC device wiring a NW Si photoanode to a PVK|Cu$_{NF}$ photocathode. **b**–**d**, SEM images of the Si$_{NW}$ array photoanode: cross-section (**b**), top view of NW array (**c**) and PtAu GOR catalyst (**d**). **e**, CV traces of CO$_2$RR, GOR and OER (photo)electrodes. The sign is reversed for cathodic traces. **f,g**, FYs of Si-PVK|Cu$_{NF}$ PEC devices with different Cu$_{NF}$ geometric areas for CO$_2$ reduction (**f**) and GOR (**g**). The high photocurrent and early onset potential of the Si$_{NW}$ photoanode shifts the bias-free operating point of PEC devices to 0.1–0.2 V versus RHE. As a result, the C$_2$ hydrocarbon

selectivity resembles that of PVK|Cu$_{NF}$ electrodes at 0 V versus RHE (Fig. 3b). **h**, CPE of a Si$_{NW}$-PVK|Cu$_{NF}$ (4 mm^2) device. **i**, CV traces of Si-PVK|Cu$_{NF}$ devices with different Cu$_{NF}$ areas. Two-hour CPE is performed at 0 V applied bias under 1 sun irradiation (AM1.5 G, 100 mW cm^{-2}), at room temperature, under stirring. A bipolar membrane separates the CO$_2$ saturated 0.1 M KHCO$_3$ solution (pH 6.8) on the cathodic side from a 1 M KOH, 0.1 M glycerol solution (pH 13.7) in the anodic compartment. In **e** and **i**, lighter shades indicate chopped light CV traces. Average values were calculated from sample triplicates, with error bars corresponding to the standard deviation.

of roughly −0.5 V versus RHE on the Cu$_{NF}$ catalyst. Due to the 0.4 V versus RHE onset of BiVO$_4$, the PEC tandem could sustain an unassisted steady-state photocurrent density of only 0.12 mA cm^{-2}. Four-hour CPE of the perovskite–BiVO$_4$ tandem at 0 V applied bias confirmed that the system could indeed produce ethane and ethylene at FYs of 0.49% and 0.18%, respectively (Fig. 4b,c). This result was in line with selectivities obtained from CPE of a PVK|Cu$_{NF}$ photocathode at 0.5 V versus RHE, or Cu$_{NF}$ electrodes at −0.5 V versus RHE (Figs. 2 and 4, Supplementary Fig. 18 and Supplementary Table 6). A lower selectivity was again obtained over a longer 10 h experiment (Supplementary Fig. 26). No O$_2$ could be detected via GC analysis owing to interference from air leakage and low product rates at absolute photocurrents of ~30 μA (quantitative O$_2$ evolution has been previously confirmed for similar tandem devices[26]).

NW TiO$_2$ photoanodes were also tested in the tandem artificial leaf configuration. While its wider bandgap limits the overall photocurrent, TiO$_2$ possesses an earlier onset potential of 0.2 V versus RHE for O$_2$ evolution, as well as an improved fill factor. The latter resulted in an increased overlap between the cathodic and anodic CV traces at ~0.45 V versus RHE, which yielded a higher bias-free photocurrent of up to 0.3 mA cm^{-2} (Fig. 4d and Supplementary Figs. 26–29). Due to the minor shift in the working potential, C$_2$ selectivity remained similar over 10 h CPE at 0 V applied bias (Supplementary Fig. 26 and Supplementary

Table 8), while the C$_2$ hydrocarbon amount only increased 1.8-fold over that of a PVK|Cu$_{NF}$–BiVO$_4$ device.

These results demonstrate that tandem PEC devices are in principle compatible with the challenging C$_2$ hydrocarbon synthesis. However, the partial C$_2$ photocurrent density remains below 0.8 μA cm^{-2}, as O$_2$ evolution demands over 1.23 V versus RHE, while substantial ethylene production typically occurs at more negative applied potentials of −0.6 to −1.1 V versus RHE[13]. Hence, further photovoltage gains, lower catalyst overpotentials and improved selectivities are still needed for practical uses. These may be attained by taking into account the optimal local environment of nanosized Cu catalysts[8,12,33,34], or introducing wide-bandgap perovskite[43,44] and buried multijunction photocathodes[45] with photovoltages >1.5 V. Alternatively, the OER can be replaced by organic oxidations with early onset potentials of ~0.3 V versus RHE[20,21], as described next (Supplementary Note 3 and Supplementary Tables 11 and 12).

PEC devices for value-added chemicals
To overcome the thermodynamic limitations of water oxidation, perovskite photocathodes were next wired to Si photoanodes with a 37.8 mm^2 active area for GOR (Fig. 5a)[20]. Both electrodes were irradiated in parallel, with the cathodic and anodic compartments separated by

a bipolar membrane. Photocurrent densities ($J_{photo,PVK}$) are reported relative to the perovskite area for consistency. Planar and NW p⁺n-Si substrates were coated with a 10-nm-thin TiO_2 layer to prevent NW degradation in the basic anodic solution. PtAu clusters were co-sputtered onto the compact TiO_2 layer, as confirmed by SEM and energy-dispersive X-ray (EDX) spectroscopy mapping (Methods, Fig. 5b–d and Supplementary Figs. 30 and 31). The resulting planar and NW p⁺n-Si|TiO_2|PtAu electrodes are abbreviated Si_p and Si_{NW}, respectively.

Both Si_p and Si_{NW} photoanodes displayed high photocurrent densities of around 10 mA cm⁻² (relative to Si area) and early onset potentials of 0 V versus RHE (Supplementary Figs. 32–34), comparable to those of state-of-the-art GOR photoanodes[20]. This resulted in an excellent overlap of the Si and perovskite CV traces at 0.1–0.2 V versus RHE, and a very early onset bias voltage of −1.2 V for the combined PEC device (Fig. 5e,i). In this case, the overall device photocurrent was limited by the perovskite photocathodes and, hence, by the Cu_{NF} geometric area (Supplementary Fig. 32). As a result, unassisted Si_p-PVK|Cu_{NF} devices displayed similar photocurrents (2–4 mA cm⁻²) and CO_2RR selectivities to those of perovskite electrodes at 0 V versus RHE (Fig. 3a,b). A C_2 hydrocarbon FY of ~1% was observed for a 40 mm² Cu_{NF} active area, which increased to 5–7% with a 4 mm² Cu_{NF} active area. On the anodic side, the Si_p photoanode yielded glycerate (53 ± 1% FY), formate (18 ± 4% FY), lactate (8 ± 1% FY) and acetate (7 ± 2% FY) as the main liquid GOR products (Fig. 5f,g, Supplementary Figs. 35–37 and Supplementary Table 9).

Si_p-PVK|Cu_{NF} and Si_{NW}-PVK|Cu_{NF} devices displayed similar selectivities and initial photocurrents. The latter sustained a steady photocurrent over 2 h CPE at 0 V applied bias and higher cumulative product amounts (Fig. 5h and Supplementary Fig. 36). This improvement is due to the Si_{NW} array geometry, yielding an improved fill factor, a higher surface area and reduced mass transport limitations, as shown from the decreased hysteresis in the CV scans (Supplementary Fig. 34). The Si semiconductor provided a 0.45 V photovoltage shift over the CV trace of PtAu deposited on carbon paper (Fig. 5e and Supplementary Figs. 38 and 39). The latter only overlaps with the PVK|Cu_{NF} trace at an operating potential of 0.48 V and current of 0.3 mA cm⁻², similar to those of perovskite–$BiVO_4$ tandem devices (Supplementary Fig. 38), indicating that a second light absorber is essential for C_2 hydrocarbon synthesis at practical rates. Accordingly, the partial C_2 photocurrent densities of Si_{NW}-PVK|Cu_{NF} (4 mm²) devices attained 155 μA cm⁻², a 200-fold improvement over those of perovskite–$BiVO_4$ artificial leaves coupling C_2 hydrocarbon production to water oxidation, whereas the total and C_2 hydrocarbon solar-to-chemical efficiencies increased twofold, reaching 0.212% and 0.0017%, respectively (Supplementary Tables 10 and 13, and Supplementary Note 3). Hence, GOR contributes substantially to unassisted PEC performance, providing a practical alternative to further CO_2RR catalyst development (Supplementary Note 3).

Conclusions

This work demonstrates PEC hydrocarbon synthesis by interfacing a hierarchically structured Cu nanoflower catalyst with a high-photovoltage perovskite light absorber. Their relative areas and respective local current densities are key to steering the C_2 hydrocarbon selectivity, which indicates the versatility of integrated PEC systems over classical semiconductor–liquid junction photoelectrodes. The C_2 selectivity of perovskite–$BiVO_4$ PEC artificial leaves can be further increased by targeting thermodynamically favourable organic oxidations. Accordingly, unassisted perovskite–Si PEC devices coupling aqueous CO_2 reduction to glycerol oxidation attain ethane and ethylene FYs between 5% and 10%, matching the optimal selectivity observed for Cu nanoflower electrodes. These results provide a proof-of-concept demonstration for simultaneous multicarbon synthesis and biomass-derived waste conversion into value-added products, which may ultimately contribute towards a sustainable fuel and chemical economy.

Methods
Materials

Cu foil (0.1 mm and 0.25 mm, Puratronic, 99.9999%, Alfa Aesar), H_3PO_4 (≥85%, Sigma-Aldrich), $(NH_4)_2S_2O_8$ (98+%, Acros), FTO glass (~7 Ω sq⁻¹, Sigma-Aldrich), Zn dust (<10 μm, ≥98%, Sigma-Aldrich), $Ni(NO_3)_2\cdot6H_2O$ (99.999%, Sigma-Aldrich), ethylene glycol (99.8%, anhydrous, Sigma-Aldrich), ethylenediamine (absolute, ≥99.5%, Sigma-Aldrich), poly[bis(4-phenyl)(2,4,6-trimethylphenyl)amine] (PTAA; molecular weight (M_w) = 17,700, EM INDEX), 2,3,5,6-tetrafluoro-7,7,8,8-tetracyanoquinodimethane (F4TCNQ, 97%, Sigma-Aldrich), PbI_2 (99.99%, for perovskite precursor, TCI), $PbBr_2$ (for perovskite precursor, TCI), formamidinium iodide (Dyesol), methylammonium bromide (Dyesol), N,N-dimethylformamide (anhydrous, 99.8%, Sigma-Aldrich), dimethyl sulfoxide (DMSO; ACS reagent, ≥99.9%), 1-methyl-2-pyrrolidone (99.5%, extradry over molecular sieves, ACROS), chloroform (99.9%, extradry over molecular sieves, ACROS), [6,6]-phenyl C_{61} butyric acid methyl ester ([60]PCBM; >99%, Ossila), chlorobenzene (extradry over molecular sieves ≥99.5%, ACROS), polyethylenimine (PEIE; 80% ethoxylated solution, 35–40 wt.% in H_2O, average M_w = 70,000, Sigma-Aldrich), isopropanol (≥99.5%, Honeywell), graphite (powder, <20 μm, synthetic, Sigma-Aldrich), H_2SO_4 (≥95%, Fisher), H_2O_2 (>30%, Fisher and EMD Millipore), $Bi(NO_3)_3\cdot5H_2O$ (98%, Sigma-Aldrich), NaI (≥99%, laboratory reagent grade, Fischer), p-benzoquinone (≥98%, Sigma-Aldrich), ethanol (absolute, VWR), vanadyl acetylacetonate (VO(acac)₂; 98.0%, Sigma-Aldrich), NaOH (analytical reagent grade, Fisher, and ≥97.0%, pellets, Sigma-Aldrich), titanium(IV) butoxide (≥97.0%, Sigma-Aldrich), HCl (37%, Sigma-Aldrich), K_2CO_3 (Puratronic, 99.997%, Thermo Scientific), CO_2 (99.999%, Linde plc), ¹³CO_2 (99.0 atom%, Sigma-Aldrich), $K_2$¹³CO_3 (98%, Cambridge Isotope Laboratories), D_2O (D 99.9%, Cambridge Isotope Laboratories), Si wafers (6″, <100> oriented, 1–10 Ω cm, prime, single sided-polished, Addison Semiconductor Materials) and carbon paper (Sigracet 29 AA, FuelCellStore) were used as purchased without further purification.

Cu_{NF} catalyst synthesis

The Cu_{NF} synthesis was adapted from literature reports[23] and further optimized for this study. The surface of flattened Cu foil was first cleaned with ethanol and manually polished using wet sandpaper (SiC, 1,200 Grit), followed by sonicating steps in acetone and water to remove residues. The foil was next electropolished in 85% H_3PO_4, by applying an anodic voltage of 5 V for 10 min against a Ti foil with a d.c. power supply (absolute current of ~0.4 A). Two solutions were prepared in separate vials by sonicating 1.369 g $(NH_4)_2S_2O_8$ in 9 ml H_2O and 4.8 g NaOH in 12 ml H_2O, respectively. The freshly dissolved solutions were mixed inside a jar with an additional 18 ml H_2O, before placing the electrodeposited Cu foil at the centre of the closed jar. CuO nanoflower growth occurred over 135 min. The foils were gently rinsed with Milli-Q water, and the nanoporous CuO layer was scrubbed from one side to enable electrical contact. The CuO-covered foils were then reduced to Cu_{NF} by applying a potential of −0.2 V versus RHE for 20–40 min, in a three-electrode configuration with a Ag/AgCl reference electrode and a Pt wire counter electrode, in 0.1 M $KHCO_3$, under air.

Perovskite photocathodes

Perovskite PV cells were first deposited by adapting reported procedures[26,27]. First, 13 × 13 mm² FTO-coated glass substrates were masked with adhesive tape and etched using Zn powder and 2 M HCl. The patterned FTO substrates were next cleaned for 10 min in Piranha solution, obtained by adding one volumetric part of 30% H_2O_2 to three parts of H_2SO_4. A solution of 1.0 M $Ni(NO_3)_2\cdot6H_2O$ and 1.0 M ethylenediamine in ethylene glycol was spin-coated on the FTO substrates at 5,000 rpm for 45 s, and then annealed at 573 K for 1 h to form a NiO_x hole transport layer. Under inert atmosphere, 111 μl from a 1 mg ml⁻¹ F4TCNQ solution in chlorobenzene was added to a 5.56 mg PTAA solution in 1 ml toluene, resulting in a 5 mg ml⁻¹ PTAA solution with 2%

F4TCNQ doping. This solution was dynamically spin-coated onto the FTO|NiO$_x$ substrates at 4,000 rpm for 30 s, then annealed at 383 K for 10 min to form a second PTAA:F4TCNQ hole transport layer. A 1.5 M CsI solution in DMSO (24 μl) was next added to a 1.0 M FAMA$_{0.22}$Pb$_{1.32}$I$_{3.2}$Br$_{0.66}$ solution in N,N-dimethylformamide (255 μl), DMSO (170 μl) and 1-methyl-2-pyrrolidone (75 μl). This triple-cation mixed-halide perovskite solution was spin-coated in two steps at 1,000 rpm for 10 s and 6,000 rpm for 35 s, whereas 75 μl of chloroform was drop cast as antisolvent before the last 7 s. The samples were next annealed at 373 K for 30 min, before spin-coating a 35 mg ml^{-1} PCBM solution in chlorobenzene at 3,000 rpm for 45 s as the electron transport layer. Samples were briefly taken outside the glovebox to coat a 3.87 μl ml^{-1} PEIE solution in isopropanol at 3,000 rpm for 30 s. A 100 nm silver layer was evaporated on top of the device stack with a photoactive area of ~25 mm^2, which was manually determined. Copper foils with a Cu$_{NF}$ catalyst were attached to the silver contacts using graphite epoxy paste. The conductive encapsulant was prepared by blending graphite powder with Araldite Standard epoxy in a 3:4 mass ratio. An insulated wire was attached to this photocathode using Ted Pella fast-drying silver paint, whereas Araldite 5-Minute Rapid epoxy was used to seal any exposed edges or wiring. The resulting photocathodes are compatible with alternative encapsulation methods including epoxy and ultraviolet curing resins, chemical vapor deposition (CVD) of micrometre-thin parylene-C coatings[27], or rubber O-rings[46].

BiVO$_4$ photoanodes

BiVO$_4$ photoanodes were prepared following reported protocols[41,47]. Patterned FTO slides were again obtained by masking and etching the substrates, before their cleaning in Piranha solution. A clear, red 0.02 M Bi(NO$_3$)$_3$·5H$_2$O, 0.4 M NaI solution was made by dispersing the two salts with an ultrasonic probe in 20 ml of Milli-Q water, followed by pH adjustment to 1.20 using concentrated HNO$_3$. A second solution consisted of 0.3 M p-benzoquinone sonicated in ethanol (9 ml). These two precursor solutions were mixed for BiOI electrodeposition. BiOI was deposited onto the FTO substrates in two steps, by applying potentials of −0.3 V versus Ag/AgCl for 5 s and −0.1 V versus Ag/AgCl for 180 s. Then, 40 μl cm^{-2} of a VO(acac)$_2$ solution in DMSO was drop cast onto BiOI samples, before annealing them for 1 h at 723 K (1 K min^{-1} ramp rate). Samples were next stirred in a 0.2 M NaOH solution to remove the residual V$_2$O$_5$. A 4.8 mg ml^{-1} [Ti$_4$O(OEt)$_{15}$(CoCl)] single-source precursor solution in dry toluene was finally spin-coated in air to form the water oxidation catalyst.

TiO$_2$ photoanodes

NW TiO$_2$ arrays were grown onto FTO glass via hydrothermal synthesis[42]. Before the deposition, the Teflon liner of a 50 ml autoclave was cleaned in aqua regia. Then, 0.5 ml of titanium(IV) butoxide was added to a solution of 37% HCl (15 ml) and H$_2$O (15 ml), and the mixture was stirred for 20−30 min. This solution was poured into the autoclave, and cleaned FTO substrates were placed inside in a tilted position. Substrates were completely immersed in the precursor solution, with the conductive FTO layer facing down. The autoclave was next placed in an oven at 443 K for 5 h. The cooled samples were rinsed with Milli-Q water and further annealed at 673 K for 1 h.

Fabrication of n-Si$_{NW}$ substrates

Si$_{NW}$ substrates were prepared following reported procedures[8,20]. N-type phosphorus-doped Si wafers were immersed in a 4.9% HF bath for 3 min to remove the native silica layer, then thoroughly washed under deionized water and dried. During a typical photoresist process, hexamethyldisilazane was applied for 2 min, then MiR 701 photoresist was spin-coated to form a 1-μm-thick layer. The surface was next patterned using a 5× i-line photolithography stepper (GCA 8500), which used a mask patterned with a square lattice of 3.75 μm circles and 10 μm pitch, to yield a final resist pattern of 0.75 μm circles and 2 μm pitch.

The pattern was next developed using MF-26A for 60 s, descummed with O$_2$ plasma at 50 W for 60 s and hard baked at 413 K with ultraviolet light. A low-frequency inductive-coupled plasma deep reaction-ion etch process was used to etch the wafer (Surface Technology Systems Advanced Silicon Etch). The process used O$_2$ and SF$_6$ as etch gas, C$_4$F$_8$ as passivation gas and a typical deep reaction-ion etch smooth-wall recipe to obtain 21-μm-long NWs. Any photoresist rests were removed under O$_2$ plasma at 250 W for 7.5 min.

Fabrication of p$^+$n-Si$_p$|TiO$_2$ and p$^+$n-Si$_{NW}$|TiO$_2$ substrates

A 6″ silicon wafer was used as the dopant carrier wafer. All wafers were cleaned in a 4.9% HF bath for 3 min, then thoroughly washed with deionized water and dried. The carrier wafer was spin-coated with a gallium silicate spin-on-dopant solution (Filmtronics) at 2,200 rpm for 30 s, then baked on a hotplate at 423 K for 30 min. N-type phosphorus-doped Si wafers or n-Si$_{NW}$ substrates were cleaned with HF, water and acetone, then placed gently onto the carrier wafer such that the polished surface touches the dopant layer, and finally placed into a rapid thermal annealing chamber at 1,173 K for 100 s under N$_2$. The resulting p$^+$n-Si$_p$ and p$^+$n-Si$_{NW}$ substrates were again cleaned with HF, water and acetone, before depositing a 10 nm TiO$_2$ layer at 473 K using atomic layer deposition with a tetrakis(dimethylamido)titanium precursor (Cambridge Fiji 200 Plasma ALD system). The cooled substrates were stored under air[20].

Si and carbon paper (photo)anodes for GOR

The PtAu catalyst was deposited using an in-house built, multitarget co-sputtering system with 3 × 3″ TORUS Mag Keeper sputter guns, two 2 kW pulsed d.c. power supplies and one 1.5 kW d.c. power supply. A ~4-nm-thick PtAu layer was co-sputtered onto p$^+$n-Si$_p$|TiO$_2$ substrates and both sides of the carbon paper, by applying 50 W power on the Pt target and 28 W power on the Au target over 15 s. Alternatively, a ~11-nm-thick layer of PtAu was co-sputtered onto p$^+$n-Si$_{NW}$|TiO$_2$ substrates, with 50 W power on the Pt target and 28 W power on the Au target for 45 s. The carbon|PtAu electrodes, p$^+$n-Si$_p$|TiO$_2$|PtAu and p$^+$n-Si$_{NW}$|TiO$_2$|PtAu substrates were stored under air until use. The Si substrates were later scratched with a Ga−In eutectic, coated with silver paint, and attached on titanium foil using double-sided conductive carbon tape. The resulting Si photoanodes were dried for 30 min under air before mounting onto the PEC cell[20].

(Photo)electrochemical characterization

Solar cells, photoelectrodes and PEC devices were characterized using a Biologic VSP potentiostat and Newport 67005 solar light simulators with AM1.5 G optical filters. The light intensity was calibrated to 1 sun (100 mW cm^{-2}) using a certified Thorlabs PM16-405 USB Power Meter. CV and CPE experiments were performed in a 0.1 M KHCO$_3$ buffer solution, pH 6.8, under stirring at room temperature unless otherwise stated. The working electrode compartment of the PEC reactor was purged for 30 min with pure CO$_2$ before experiments. Photoelectrodes were characterized in a two-compartment, three-electrode configuration with a Ag/AgCl/KCl$_{(1 M)}$ (CH Instruments CHI111) reference and a platinum mesh counter electrode. Selemion AMV (AGC Engineering), a standard anion exchange membrane for CO$_2$ reduction under neutral pH, separated the anodic and cathodic compartments. This membrane allows anion transport between compartments, preventing the build-up of pH differences. Applied potentials were determined using the equation E (V versus RHE) = E (V versus Ag/AgCl) + 0.059 V × pH + 0.230 V (298 K). The potentials were not IR corrected, unless otherwise specified. CO$_2$RR−OER tandem devices were investigated in a two-electrode, single-compartment configuration. J−V scans of solar cells were recorded between −0.1 V and 1.2 V (100 mV s^{-1} scan rate, 20 mV step size). CV was typically performed between −0.9 V and 0 V versus RHE for the Cu$_{NF}$ electrodes, −0.2 V and 1.0 V versus RHE for PVK|Cu$_{NF}$ photocathodes, 0.1 V and 1.4 V versus RHE for photoanodes and −0.7 V and 0.8 V for PEC tandems (10 mV s^{-1}

scan rate). No masking was used for solar cells and photoelectrodes, whereas the active area of photoanodes was surrounded by opaque tape for PEC tandem devices (Supplementary Fig. 40). Geometric areas of each (photo)electrode were measured with 0.5 mm precision for perovskite light absorbers and 0.1 mm precision for Cu_{NF} catalysts, which amounts to a measurement uncertainty <10%, within common experimental error. For CO_2RR–GOR devices, the Si photoanode was mounted on the back wall using an x-ring defining a 37.8 mm^2 photoactive area. The anodic compartment contained 1 M KOH, 0.1 M glycerol solution (pH 13.7) under air and was separated from the cathodic side by a bipolar membrane (Fumasep), which is necessary for solutions of different pH values.

Product quantification

Gaseous products were typically accumulated in the extended headspace of a PEC reactor over 2 h CPE tests (Supplementary Fig. 41). Three millilitres of the headspace were injected in an Agilent 7890B gas chromatograph. CO, C_2H_4 and C_2H_6 quantification was performed using a flame ionization detector (see example traces in Supplementary Fig. 42). A thermal conductivity detector was used for H_2, N_2 and O_2 detection. However, the small amounts of O_2 produced by tandem devices under unassisted operation (~1.1 µmol, or 27 µl) could not be detected due to interferences from atmospheric O_2. Apparent gas leakage remained below 10% of the headspace, including product losses during gas sampling and transfer. An SRI MG3 gas chromatograph was used for product quantification under CO_2 flow, which was set to 5 sccm using an Omega Engineering FMA5508 gas mass flow controller. ^{13}C isotope measurements were carried out on a Waters AutoSpec Premier GC–MS with 0.0002 m/z resolution. Liquid product quantification was performed via water suppression ^1H NMR spectroscopy on a 600 Hz Bruker AV600 equipment. For this purpose, 10 vol.% of a D_2O–DMSO standard was added to the analyte solution. The standard solution was prepared by adding 400 µl DMSO to 100 g of D_2O (refs. [8],[20],[48]).

Materials characterization

SEM images and EDX mapping were recorded using a Zeiss Gemini Ultra-55. X-ray photoelectron spectroscopy was performed on a Thermo Scientific K-Alpha instrument using an Al Kα source. A spot size of 400 µm and a pass energy of 50 eV were used. XRD data were collected using a Bruker D8 laboratory diffractometer with a Cu Kα radiation source in ambient condition. Data were collected from $2\theta = 10°$ to 90° with a step size of 0.02941692° per step and time per step of 1 s.

Statistics

Averaged values are calculated from sample triplicates, whereas measurement errors and error bars correspond to the standard deviation.

Data availability

The raw data that support the findings of this study are available via Apollo, the University of Cambridge data repository, at https://doi.org/10.17863/CAM.114522 (ref. [49]).

References

1. de Luna, P. et al. What would it take for renewably powered electrosynthesis to displace petrochemical processes? *Science* **364**, eaav3506 (2019).
2. Joya, K. S., Joya, Y. F., Ocakoglu, K. & van de Krol, R. Water-splitting catalysis and solar fuel devices: artificial leaves on the move. *Angew. Chem. Int. Ed.* **52**, 10426–10437 (2013).
3. Sokol, K. P. & Andrei, V. Automated synthesis and characterization techniques for solar fuel production. *Nat. Rev. Mater.* **7**, 251–253 (2022).
4. Speight, J. G. *Handbook of Industrial Hydrocarbon Processes* (Gulf Professional Publishing, 2011).
5. de Luna, P. et al. Catalyst electro-redeposition controls morphology and oxidation state for selective carbon dioxide reduction. *Nat. Catal.* **1**, 103–110 (2018).
6. Wakerley, D. et al. Gas diffusion electrodes, reactor designs and key metrics of low-temperature CO_2 electrolysers. *Nat. Energy* **7**, 130–143 (2022).
7. Huang, J. E. et al. CO_2 electrolysis to multicarbon products in strong acid. *Science* **372**, 1074–1078 (2021).
8. Roh, I. et al. Photoelectrochemical CO_2 reduction toward multicarbon products with silicon nanowire photocathodes interfaced with copper nanoparticles. *J. Am. Chem. Soc.* **144**, 8002–8006 (2022).
9. Kempler, P. A., Richter, M. H., Cheng, W.-H., Brunschwig, B. S. & Lewis, N. S. Si microwire-array photocathodes decorated with Cu allow CO_2 reduction with minimal parasitic absorption of sunlight. *ACS Energy Lett.* **5**, 2528–2534 (2020).
10. Nitopi, S. et al. Progress and perspectives of electrochemical CO_2 reduction on copper in aqueous electrolyte. *Chem. Rev.* **119**, 7610–7672 (2019).
11. Hori, Y., Wakebe, H., Tsukamoto, T. & Koga, O. Electrocatalytic process of CO selectivity in electrochemical reduction of CO_2 at metal electrodes in aqueous media. *Electrochim. Acta* **39**, 1833–1839 (1994).
12. Kim, D., Kley, C. S., Li, Y. & Yang, P. Copper nanoparticle ensembles for selective electroreduction of CO_2 to C_2–C_3 products. *Proc. Natl Acad. Sci. USA* **114**, 10560–10565 (2017).
13. Ren, D., Fong, J. & Yeo, B. S. The effects of currents and potentials on the selectivities of copper toward carbon dioxide electroreduction. *Nat. Commun.* **9**, 925 (2018).
14. Yang, W., Prabhakar, R. R., Tan, J., Tilley, S. D. & Moon, J. Strategies for enhancing the photocurrent, photovoltage, and stability of photoelectrodes for photoelectrochemical water splitting. *Chem. Soc. Rev.* **48**, 4979–5015 (2019).
15. Lim, H. et al. High performance III-V photoelectrodes for solar water splitting via synergistically tailored structure and stoichiometry. *Nat. Commun.* **10**, 3388 (2019).
16. Andrei, V. et al. Long-term solar water and CO_2 splitting with photoelectrochemical BiOI–$BiVO_4$ tandems. *Nat. Mater.* **21**, 864–868 (2022).
17. Luo, J. et al. Cu_2O nanowire photocathodes for efficient and durable solar water splitting. *Nano Lett.* **16**, 1848–1857 (2016).
18. Andrei, V., Roh, I. & Yang, P. Nanowire photochemical diodes for artificial photosynthesis. *Sci. Adv.* **9**, eade9044 (2023).
19. Rahaman, M. et al. Solar-driven liquid multi-carbon fuel production using a standalone perovskite–$BiVO_4$ artificial leaf. *Nat. Energy* **8**, 629–638 (2023).
20. Lin, J.-A., Roh, I. & Yang, P. Photochemical diodes for simultaneous bias-free glycerol valorization and hydrogen evolution. *J. Am. Chem. Soc.* **145**, 12987–12991 (2023).
21. Bhattacharjee, S. et al. Reforming of soluble biomass and plastic derived waste using a bias-free $Cu_{30}Pd_{70}$|perovskite|Pt photoelectrochemical device. *Adv. Funct. Mater.* **32**, 2109313 (2022).
22. Wang, L. et al. Selective reduction of CO to acetaldehyde with CuAg electrocatalysts. *Proc. Natl Acad. Sci. USA* **117**, 12572–12575 (2020).
23. Wang, L. et al. Electrochemically converting carbon monoxide to liquid fuels by directing selectivity with electrode surface area. *Nat. Catal.* **2**, 702–708 (2019).
24. Suter, S. & Haussener, S. Optimizing mesostructured silver catalysts for selective carbon dioxide conversion into fuels. *Energy Environ. Sci.* **12**, 1668–1678 (2019).
25. Hall, A. S., Yoon, Y., Wuttig, A. & Surendranath, Y. Mesostructure-induced selectivity in CO_2 reduction catalysis. *J. Am. Chem. Soc.* **137**, 14834–14837 (2015).

26. Andrei, V., Reuillard, B. & Reisner, E. Bias-free solar syngas production by integrating a molecular cobalt catalyst with perovskite–BiVO$_4$ tandems. *Nat. Mater.* **19**, 189–194 (2020).

27. Andrei, V. et al. Floating perovskite–BiVO$_4$ devices for scalable solar fuel production. *Nature* **608**, 518–522 (2022).

28. Li, C. W. & Kanan, M. W. CO$_2$ reduction at low overpotential on Cu electrodes resulting from the reduction of thick Cu$_2$O films. *J. Am. Chem. Soc.* **134**, 7231–7234 (2012).

29. Yang, K. D. et al. Morphology-directed selective production of ethylene or ethane from CO$_2$ on a Cu mesopore electrode. *Angew. Chem. Int. Ed.* **56**, 796–800 (2017).

30. Xiang, K. et al. Microenvironmental feeding and stabilization of C$_2$H$_4$ intermediates by iodide-doped copper nanowire arrays to boost C$_2$H$_6$ formation. *Energy Fuels* **35**, 15987–15994 (2021).

31. Vasileff, A. et al. Electrochemical reduction of CO$_2$ to ethane through stabilization of an ethoxy intermediate. *Angew. Chem. Int. Ed.* **59**, 19649–19653 (2020).

32. Kuhl, K. P., Cave, E. R., Abram, D. N. & Jaramillo, T. F. New insights into the electrochemical reduction of carbon dioxide on metallic copper surfaces. *Energy Environ. Sci.* **5**, 7050–7059 (2012).

33. Li, Y. et al. Electrochemically scrambled nanocrystals are catalytically active for CO$_2$-to-multicarbons. *Proc. Natl Acad. Sci. USA* **117**, 9194–9201 (2020).

34. Yang, Y. et al. Operando studies reveal active Cu nanograins for CO$_2$ electroreduction. *Nature* **614**, 262–269 (2023).

35. Cheng, W.-H. et al. CO$_2$ reduction to CO with 19% efficiency in a solar-driven gas diffusion electrode flow cell under outdoor solar illumination. *ACS Energy Lett.* **5**, 470–476 (2020).

36. Kong, Q. et al. Directed assembly of nanoparticle catalysts on nanowire photoelectrodes for photoelectrochemical CO$_2$ reduction. *Nano Lett.* **16**, 5675–5680 (2016).

37. Luo, J. et al. Water photolysis at 12.3% efficiency via perovskite photovoltaics and Earth-abundant catalysts. *Science* **345**, 1593–1596 (2014).

38. King, A. J., Bui, J. C., Bell, A. T. & Weber, A. Z. Establishing the role of operating potential and mass transfer in multicarbon product generation for photoelectrochemical CO$_2$ reduction cells using a Cu catalyst. *ACS Energy Lett.* **7**, 2694–2700 (2022).

39. Hori, Y., Murata, A. & Takahashi, R. Formation of hydrocarbons in the electrochemical reduction of carbon dioxide at a copper electrode in aqueous solution. *J. Chem. Soc. Faraday Trans. 1* **85**, 2309–2326 (1989).

40. Kas, R., Kortlever, R., Yılmaz, H., Koper, M. T. M. & Mul, G. Manipulating the hydrocarbon selectivity of copper nanoparticles in CO$_2$ electroreduction by process conditions. *ChemElectroChem* **2**, 354–358 (2015).

41. Kim, T. W. & Choi, K.-S. Nanoporous BiVO$_4$ photoanodes with dual-layer oxygen evolution catalysts for solar water splitting. *Science* **343**, 990–994 (2014).

42. Hwang, Y. J., Hahn, C., Liu, B. & Yang, P. Photoelectrochemical properties of TiO$_2$ nanowire arrays: a study of the dependence on length and atomic layer deposition coating. *ACS Nano* **6**, 5060–5069 (2012).

43. Arora, N. et al. High open-circuit voltage: fabrication of formamidinium lead bromide perovskite solar cells using fluorene–dithiophene derivatives as hole-transporting materials. *ACS Energy Lett.* **1**, 107–112 (2016).

44. Wu, C.-G., Chiang, C.-H. & Chang, S. H. A perovskite cell with a record-high-V$_{oc}$ of 1.61 V based on solvent annealed CH$_3$NH$_3$PbBr$_3$/ICBA active layer. *Nanoscale* **8**, 4077–4085 (2016).

45. Young, J. L. et al. Direct solar-to-hydrogen conversion via inverted metamorphic multi-junction semiconductor architectures. *Nat. Energy* **2**, 17028 (2017).

46. Daboczi, M., Cui, J., Temerov, F. & Eslava, S. Scalable all-inorganic halide perovskite photoanodes with >100 h operational stability containing Earth-abundant materials. *Adv. Mater.* **35**, 2304350 (2023).

47. Andrei, V. et al. Scalable triple cation mixed halide perovskite–BiVO$_4$ tandems for bias-free water splitting. *Adv. Energy Mater.* **8**, 1801403 (2018).

48. Chen, C. et al. Exploration of the bio-analogous asymmetric C–C coupling mechanism in tandem CO$_2$ electroreduction. *Nat. Catal.* **5**, 878–887 (2022).

49. Andrei, V. et al. Perovskite-driven solar C$_2$ hydrocarbon synthesis from CO$_2$. *Apollo* https://doi.org/10.17863/CAM.114522 (2025).

Acknowledgements

Author contributions

V.A., I.R. and P.Y. designed the project. V.A., I.R. and J.-A.L. conducted the (photo)electrochemical characterization. V.A. fabricated the perovskite solar cells and BiVO$_4$ photoanodes. C.-K.L. and S.S. assisted with metal evaporation and device fabrication. I.R. and J.L. synthesized the Cu flower catalyst. J.-A.L. fabricated the TiO$_2$ photoanodes. J.-A.L. and I.R. prepared and characterized the Si GOR photoanodes. Y.S. recorded SEM and EDX data of Si GOR photoanodes. V.A. and I.R. drafted the paper. V.A., I.R., J.-A.L., J.L., Y.S., C.-K.L., S.S., E.R. and P.Y. contributed to the discussion, revision and completion of the paper.

Competing interests

The authors declare no competing interests.

Additional information

Supplementary information The online version contains supplementary material available at https://doi.org/10.1038/s41929-025-01292-y.

Correspondence and requests for materials should be addressed to Virgil Andrei or Peidong Yang.

Peer review information *Nature Catalysis* thanks Gengfeng Zheng and the other, anonymous, reviewer(s) for their contribution to the peer review of this work.

Reprints and permissions information is available at www.nature.com/reprints.